Anthropogenic emissions and urbanization increase risk of compound hot hot extremes in cities

Citation for published version:
Wang, J, Chen, Y, He, G, Tett, S, Yan, Z, Zhai, P, Feng, J, Ma, W, Huang, C & Hu, Y 2021, 'Anthropogenic emissions and urbanization increase risk of compound hot hot extremes in cities', *Nature Climate Change*, vol. 11, pp. 1084–1089. https://doi.org/10.1038/s41558-021-01196-2

Digital Object Identifier (DOI):
10.1038/s41558-021-01196-2

Document Version:
Peer reviewed version

Published In:
Nature Climate Change

Inventory of Supporting Information

Manuscript #: NCLIM-20092296B

Corresponding author name(s): Yang Chen, Wenjun Ma

1. Supplementary Information:

Item	**Present?**	**Filename** This should be the name the file is saved as when it is uploaded to our system, and should include the file extension. The extension must be .pdf	**A brief, numerical description of file contents.** i.e.: *Supplementary Figures 1-4, Supplementary Discussion, and Supplementary Tables 1-4.*
Supplementary Information	Yes	Supplementary_text_figure_tables.pdf	Supplementary Note 1, Supplementary Discussion 1-3, Supplementary Figures 1-14, Supplementary Tables 1-5
Reporting Summary	No		

Anthropogenic emissions and urbanization increase risk of compound hot extremes in cities

Jun Wang[1], Yang Chen[2*], Weilin Liao[3], Guanhao He[4], Simon F. B. Tett[5], Zhongwei Yan[1,6], Panmao Zhai[2], Jinming Feng[1], Wenjun Ma[7*], Cunrui Huang[8] and Yamin Hu[9]

[1]Key Laboratory of Regional Climate-Environment for Temperate East Asia (RCE-TEA), Institute of Atmospheric Physics, Chinese Academy of Sciences, Beijing, China.

[2]State Key Laboratory of Severe Weather, Chinese Academy of Meteorological Sciences, Beijing, China.

[3]School of Geography and Planning, Sun Yat-sen University, Guangzhou, China.

[4]Guangdong Provincial Institute of Public Health, Guangdong Provincial Center for Disease Control and Prevention, Guangzhou, China.

[5]School of GeoSciences, The University of Edinburgh, Edinburgh, UK.

[6]University of Chinese Academy of Sciences, Beijing, China.

[7]School of Medicine, Jinan University, Guangzhou, China

[8]Vanke School of Public Health, Tsinghua University, Beijing, China.

[9]Guangdong Climate Center, Guangzhou, China.

*Corresponding author. Email: ychen@cma.gov.cn, mawj@gdiph.org.cn

Abstract

Urban areas are experiencing strongly increasing hot extremes. However, these events have seldom been the focus of traditional detection and attribution analysis designed for regional-to-global changes. Here, we show that compound (day-night sustained) hot extremes are more dangerous than solely daytime or nighttime heat, especially to female and older urban residents. Urban compound hot extremes across Eastern China have increased by 1.76 days decade^{-1} in 1961–2014, with fingerprints of urban expansion and anthropogenic emissions detected by a stepwise detection and attribution method. Their attributable fractions are estimated as 0.51 (urbanization), 1.63 (greenhouse gases) and -0.54 (other anthropogenic forcings) days decade^{-1}. Future emissions and urbanization would make these compound events two-to-five times more frequent (2090s vs. 2010s), leading to a three-to-sixfold growth in urban population exposure. Our findings call for tailored adaptation planning against rapidly growing health threats from compound heat in cities.

Increasing and intensifying hot temperature extremes have posed severe health and socio-economic impacts[1]. Heat-related health consequences vary with characteristics of the exposed landscape and types of hot extremes. Mortality tends to be higher in urban areas, due to greater population exposure and urban heat island (UHI) effects[2,3]. Despite mounting evidence of detrimental health impacts from hot days or nights due to their high intensity and/or long duration, their occurrence in close sequence, i.e., a compound hot extreme, has received little attention but might bear disproportionately large health risks. The loss of nighttime cooling relief severely disturbs physiological responses of people well-acclimatized to the conventional hot day-cool night mode, thereby triggering mortality spikes as showcased in the 1995 Chicago and 2003 Europe events[4,5]. Given that cities are now home to more than 50% of the world's population and emit at least 70% of global greenhouse gases[6], understanding how cities impact, and are impacted by dangerous hot extremes in the context of anthropogenic climate change is fundamental to actionable planning.

This is particularly vital and urgent to densely populated and rapidly urbanizing areas like Eastern China[7]. During the past few decades, broad swathes of the region experienced a significant transition of summertime hot extremes from solely daytime or nighttime events to day-night compound hot extremes[8], with greater rates observed and projected in cities[9]. Rapid ageing of city dwellers could further enhance societal vulnerability to compound hot extremes[10]. These socio-economic, climatic, and demographic factors combine to underscore the imperative of evaluating risks of compound hot extremes over urban Eastern China, and other urbanizing regions.

A quantitative attribution of changes in urban compound hot extremes is the first step toward risk assessments, yet remains methodologically challenging. Urban-scale extremes are impacted by forcings from both large-scale drivers (e.g., globally well-mixed greenhouse gases) and local urbanization. The standard detection and attribution framework, based on coarse-resolution climate models, has long been dedicated to contributions from large-scale drivers only[11]. The metric of 'urban minus rural' in observations[12] that was preferentially used to approximate urbanization effects on extremes downplays other urban-rural contrasting forcings, such as aerosol loadings and widespread deforestation/aforestation[13]. Moreover, distinct origins of data and method should preclude any straightforward comparison between the observation-based inference and the model-based attribution[14,15]. Namely, the current understanding on these drivers remains incomplete, highlighting the need for a unified detection and attribution method that enables the quantification and comparison of global and local forcings in the same framework[16].

An accurate understanding on the vulnerability of urban population to compound hot extremes is another prerequisite to the risk assessment, but is hampered by the prevalence of univariate definition of hot extremes in both epidemiology and climate sciences. For instance, a hot day defined by a threshold-exceeding daily maximum temperature is intended for daytime-only heat, which is then believed accountable for heat-related mortality of the day[17,18]. This practice might exaggerate the impact of presumed daytime exposure because of overlooking confounding effects of the preceding (midnight-to-sunrise) or/and following (evening-to-midnight) nighttime heat. The mismatch between the exposure and vulnerability stands out in hot night analysis as well[19]. The univariate definition also hinders our ability to realize substantially differing long-term trends[8] and physical mechanisms[20] amongst daytime, nighttime and compound hot extremes, possibly leading to the process-based weather forecast and the associated heat warning deviated from the right type of events. Hence, it is worthwhile to adopt a bivariate-definitional perspective to revisit the health impact from daytime and nighttime hot extremes, both independently and interactively, to pin down the most dangerous configuration.

To gain insights into above gaps, focusing on Eastern China, we firstly re-evaluate human health impacts of urban hot extremes based on a bivariate classification. With respect to the identified most health-detrimental type, we then conduct quantitative detection and attribution of past changes based on a novel framework, and make observationally constrained projections. The outcomes provide the most comprehensive understanding, to date, on urban compound hot extremes.

Mortality risk attributed to compound hot extremes. We calculate the pooled relative risks (RRs, 1-day lag cumulative effects accounted for) of summertime hot extremes on mortality in 98 death surveillance sites covering major urban agglomerations in China (Fig. 1; see Methods). For total non-accidental mortality, the cumulative risk of compound hot extremes (best-estimated RR=1.15, 95% confidence interval [CI]: 1.13–1.17) is significantly higher than normal days (dashed line in Fig. 1), and also markedly larger than that of daytime- and nighttime-only events. The RRs of compound hot extremes remain significant and the highest across gender and age groups, with female (best-estimated=1.19, 1.16–1.22) and older adults (≥ 75 years old, best-estimated=1.20, 1.17–1.23) most at risk. This conclusion robustly holds against the consideration of longer lags (Supplementary Fig. 1) and the choice of mortality records of varying periods, locations and numbers of surveillance sites (Supplementary Table 1; see Methods). These analyses present clear evidence that compound hot extremes are more deadly than daytime- and nighttime-only events to city dwellers over Eastern China.

Faster increase in compound hot extremes in cities. Based on satellite-sensing land use/land cover maps (see Methods), urban stations are dynamically classified with time, to better characterize both the expansion of pre-existing cities and the construction of new ones. Summertime compound hot extremes are on the rise during 1961–2014 in both urban and rural areas, with larger frequency increases observed in northeast and southeast China (Supplementary Figs. 2a and 2b). A relatively small increase in the North China Plain is sandwiched in-between, possibly due to the cooling caused by intense haze pollution[21] and expanding irrigation[22]. The overall pattern is well reproduced by the multi-model ensemble (MME) mean (Supplementary Fig. 3). Urban areas have shown stronger increases in event frequency at both grid-level (Supplementary Fig. 2c) and regional-scale (Supplementary Fig. 2d), especially after the mid-1980s coincident to the start of rapid urban expansion[23].

Drivers for the increase of urban compound hot extremes. To unify regional urbanization and large-scale external forcings in the quantitative detection and attribution, we develop a stepwise framework combining observations and simulations (see Methods). The high collinearity between greenhouse gases- and urbanization-forced patterns does not allow us to attribute all signals simultaneously[24] (see Discussion).

As urbanization forcing is absent in both simulations and rural observations, as the first step, we attribute observed changes in rural-mean frequency using space-time fingerprinting (see Methods). The observed increasing trend for rural events falls within the realm of the ensemble simulations containing all known large-scale forcings (ALL; Fig. 2a), but cannot be reproduced by the simulations driven purely by natural forcings (NAT), suggesting a key role of anthropogenic forcings (ANT) in it. The two-signal analysis does detect ANT in the rural-mean series (the scaling factor excludes zero; see Methods), while the signal of NAT is non-detectable (Fig. 3a). We further disentangle the contributions from anthropogenic emissions of greenhouse gases (GHG), other anthropogenic forcings (OANT; dominated by anthropogenic aerosols and large-scale land use changes) and natural forcings (Fig. 3a). In this three-signal detection, both the forcings of GHG and OANT can be detected, and the NAT forcing remains non-detectable. The below-unity scaling factors for ANT and GHG indicate an overestimate for the amplitude of responses to GHG-dominated anthropogenic forcings in models. Forced by anthropogenic GHG alone, the increase in rural compound hot extremes, estimated at 1.63 days decade^{-1} (5–95% uncertainty range [UR]: 1.16–2.11 days decade^{-1}), should have been greater than observed (Fig. 3b). Anthropogenic aerosols and large-scale land use changes reduce the frequency by a rate of -0.49 days decade^{-1} (-0.79 – -0.21 days decade^{-1}), offsetting around 30% of GHG-induced increases. The NAT-forced frequency change is negligibly small (0.08 days decade^{-1}, -0.02–0.18 days decade^{-1}).

It is plausible to expect that the responses to GHG and NAT differ trivially in urban and rural areas at the scale of Eastern China. Hence, the urban-rural contrast in the frequency changes of compound hot extremes should be primarily due to added heat from urbanization (increased surface sensible heat and reduced evaporative cooling from incremental impervious surface), spatially heterogeneous radiative forcings from urban-rural gradient in aerosol loadings[13] and extra forcings related to large-scale land use changes (e.g., widespread deforestation). In view of this, we remove the GHG and NAT-forced frequency changes from the urban-mean series, leaving the residual expressed as a linear combination of OANT- and urbanization-induced (URB) changes (see Methods).

In this residual series, the URB fingerprint (urbanization-induced spatiotemporal changes in frequency) is assumed to scale with urban built-up areas that expanded slowly, steeply and then plateaued gradually over Eastern China, generally following an 'S'-shape pathway[15,25]. We accordingly use the S-shape logistic sigmoid function to model the process (Fig. 2b), and take the fitted part as the URB fingerprint (see Methods). Similar to the fingerprints of large-scale forcings, the URB fingerprint only serves as the first-order approximation, which needs to be further calibrated via 'optimal fingerprinting'.

Considering the URB and OANT forcings, we conduct the second-step detection and attribution with respect to the residual series (see Methods). Both the OANT and URB fingerprints can be detected in the past spatiotemporal evolutions of urban compound hot extremes, with their scaling factors consistent with the unity (Fig. 3a). The OANT-caused reduction in compound hot extremes in cities (-0.54 days decade^{-1}, 5–95% UR: -0.80 – -0.29 days decade^{-1}) is around 10% greater than that in rural areas (-0.49 days decade^{-1}, -0.79 – -0.21 days decade^{-1}), in line with the expectation of higher aerosol loadings in urban areas causing stronger radiative cooling[13]. Based on the formal attribution, urbanization has increased the event occurrence by 0.51 days decade^{-1} (0.15–0.88 days decade^{-1}), accounting for approximately 29% in the observed increase in urban-mean compound hot extremes. Whilst, the direct observational urban-minus-rural provides an estimate of urbanization-added frequency by 0.42 days decade^{-1}, underestimating the forcing of urban land expansion by around 18% (0.09 in 0.51).

The detection of the URB and OANT fingerprints in urban-mean series is robust, in both qualitative and quantitative ways, against the sampling uncertainty related to station selection/classification, the scheme of removing large-scale forcings (Supplementary Discussions 1 and 2), different lengths of smoothing window for the data pre-processing (Supplementary Fig. 4; see Methods) and alternative use of CMIP5 outputs[26] over 1961–2012 (Supplementary Fig. 5 and Table 2; see Methods).

Future exposure to urban compound hot extremes. Our analysis confirms that anthropogenic emissions (including GHG and aerosols) and urbanization are the dominant drivers for urban compound hot extremes' changes. Thus, we use observationally constrained MME mean projection plus future urbanization-added increases to estimate anthropogenically-forced frequency changes in future (see Methods). In the near term (before 2050), the frequency increases are largely independent of emissions scenarios; whereas after the mid-21st century, the choice of scenarios makes a big difference in the magnitude of increases. Under the sustainable scenario—SSP1-2.6, urban compound hot extremes are projected to increase from around 11 days in the 2010s to 26 days in the 2090s (Fig. 4a). By contrast, under a high emission scenario (SSP5-8.5), the frequency is expected to reach around 50 days (Fig. 4a). Anthropogenically-forced increases in urban compound hot extremes scale quasi-linearly with global warming levels, with every additional 1°C of global warming translating into extra 10 compound events to occur in the warmer decade, across urban Eastern China (Fig. 4b). Inferred from this significant linear relationship, future GHG-driven global warming may account for as high as 97% of total variance in future frequency increases in urban compound hot extremes there.

Apart from heat hazard increases, future risks of summertime compound hot extremes also depend on exposure, i.e., the size and spatiotemporal pattern of population (see Methods). At mid-century under SSP1-2.6, the emission-driven increases in urban compound heat hazards would bring an increase in urban population exposure of 23.5 billion person-days (Fig. 4c), relative to the 2010s level of 6.7 billion person-days. The "hot spots" for the mid-century population exposure are clustered in three large urban agglomerations, namely the Beijing-Tianjin-Hebei region, Yangtze River Delta and Pearl River Delta (Supplementary Fig. 6). Future urban expansions are projected to amplify the emissions-driven surge in population exposure by ~13% (i.e., 3.1 billion person-days) by mid-century. With the expectation of relatively mild increases in summertime compound hot extremes and a peak-then-fall urban population structure under SSP1 (Supplementary Fig. 7), the end-of-century urban population exposure might be lower than the mid-century level (Fig. 4c).

Under SSP5-8.5, GHG emissions and urban land expansion combine to increase urban population exposure by around 42 billion person-days till the end of this century. This is discernably larger than the counterparts under low-to-intermediate emissions (i.e., SSP1-2.6, SSP2-4.5; Fig. 4c). In contrast to SSP1-2.6, the emission-driven increase in heat hazards under SSP5-8.5 dominates over demographic changes in driving future growth in urban population exposure (Fig. 4c). Thus, moving to net-zero GHG emissions sooner rather than later has the potential of offering a huge health co-benefit.

For rural areas, future population exposure will decrease under most scenarios (i.e., SSP1-2.6, SSP2-4.5 and SSP5-8.5; Supplementary Fig. 8) due mainly to population migration to urban areas (Supplementary Fig. 7c). However, following a regional rivalry pathway with low priority for addressing global environmental issues (SSP3-7.0), the exposure of rural population in Eastern China, who have less access to adaptation facilities (such as air conditioning) and have to work outdoors for longer time, will also increase during the course of this century (Supplementary Fig. 8), though the magnitude is much smaller than in urban areas.

Discussion

Our results quantitatively confirm that day-night compound hot extremes are more damaging to human health than daytime- and nighttime-only events, especially to female and older (≥ 75 years old) urban residents. Fingerprints of both anthropogenic emissions (GHG and aerosols) and regional-unique urbanization are detected in increasing compound hot extremes over urban Eastern China, with GHG contributing most. The same methodological framework estimates the urbanization contribution at around 29%. Future anthropogenic emissions, continuing urbanization and demographic variations, together, lead to an approximately three-to-sixfold increase in population exposure to compound heat across urban Eastern

China by the end of the 21st century.

We avoided using the traditional single-step fingerprinting method to disentangle the signature of urbanization from GHG-dominated anthropogenic warming, since the space-time responses of hot extremes to them are strongly correlated (r>0.95) over Eastern China. This is determined by the statistical nature of the optimal fingerprinting method—multivariate linear regression, in which the multicollinearity of predictors (i.e., high correlations among fingerprints) could bias the estimate for the magnitude and significance of regression coefficients (i.e., scaling factor and uncertainty range, and accordingly the detectability and attributable fraction)[24]. We employed the variance inflation factor[27] (VIFs; see Methods) to formally measure the degree of multicollinearity among the fingerprints. As shown in Supplementary Table 3, aligning GHG and URB in a single step would yield VIFs over 10, indicative of an unacceptably high level of multicollinearity[28]. Alternatively, considering GHG+NAT+OANT, and OANT+URB separately, as we did in the newly-devised framework, restricts the multicollinearity to a reasonably low level. As a result, when considering regional-specific non-GHG forcings, the stepwise framework might be a more generalized mode.

The method design and result interpretation for detection and attribution of urbanization-like localized forcings also depend critically on explicit framing of the spatial scale. We here addressed the detectability and contribution of urbanization to changes in urban-mean event frequency, rather than the regional-mean (urban and rural combined) series. To illustrate the difference, we similarly employed the stepwise framework to the regional-mean frequency of compound hot extremes (Supplementary Fig. 9), with the URB fingerprint constructed as the difference between the regional series and rural series. In the regional increase of 1.48 days decade^{-1} (90% CI: 1.09–1.84 days decade^{-1}), URB can no longer be detected (Supplementary Fig. 9c). Therefore, it should be articulated that the signature of urbanization is only detectable in changes of urban compound hot extremes, but is still too weak to be detected in regional-mean changes over Eastern China.

Though the considered regional expansion of urban impervious surfaces is the main driver for UHI effects[29], the attributed and projected urbanization-induced increases in compound hot extremes should be communicated as conservative estimates. Other unaccounted city-dependent factors, such as urban morphological characteristics, urban anthropogenic heat (e.g., waste heat from air conditioning), aerosol reductions in cities[30] and potential nonlinear interactions between hot extremes and UHI[31], may also modulate the local UHI magnitude. Changes in strength of land-atmosphere feedbacks and in frequency of hot extreme-producing synoptic weather regimes might introduce additional uncertainty in simulating the coupling of daytime and nighttime temperature[32-34], thus propagating into future projections.

Regarding the health impact, though we moved a step forward in distinguishing compound hot extremes from singular hot days or nights, the inconsistency in the observing and archiving conventions of temperature and mortality data prohibits us from making further distinction amongst different compound sequences, i.e., midnight-to-afternoon, afternoon-to-midnight and midnight-afternoon-midnight (see Definition of summertime hot extremes). Long-term hourly temperature records, alongside hourly-to-subdaily mortality records, would allow to precisely match specific sequence of compound heat with the after-exposure health consequences[3,20,35,36]. Also worth further exploration is the added health burden from the duration dimension of compound hot extremes, which requests longer-period mortality data to match even rarer multi-day compound heat waves.

We report that the public health risks from anthropogenic increases in compound hot extremes have been increasing, and will continue to increase over urban Eastern China. The uncovered age-specific vulnerability to compound hot extremes implies further elevated health burden due to rapid ageing of urban population there. Therefore, adapting to and mitigating climate change in the urban context will achieve co-benefits and synergies between reducing heat-related health risks and getting to the committed net-zero emission goals.

Methods

Data. *Observational climatic records and land use data.* We used daily maximum (Tmax) and minimum (Tmin) temperature observations over 1961–2014 from 2,474 meteorological stations in China[37]. The dataset was compiled and quality-controlled by the China Meteorological Data Service Center, and was homogenized using the RHtestsV3 software package[38]. Stations with five or more Tmax/Tmin records missing in any summer (i.e., June, July, and August) were discarded, giving us a total of 1,788 stations over Eastern China. Individual missing values were infilled by the average of neighboring two days.

To classify urban and rural stations, we used temporally evolving land use/land cover (LULC) maps of China, generated via the Landsat Thematic Mapper/Enhanced Thematic Mapper satellite images at a 30m resolution[39]. These LULC maps were provided at six representative years: 1980, 1990, 1995, 2000, 2005 and 2010, each of which was accordingly used to represent six periods (1961–1980, 1981–1990, 1991–1995, 1996–2000, 2001–2005, and 2006–2014) (Supplementary Fig. 10). The period-specific built-up area was measured by the end-year LULC map, except for that of the last episode using the 2010 map. The built-up lands include urban facilities and infrastructures, predominately residential, industrial, commercial, and institutional lands in cities, counties and towns[40], with a tiny proportion comprising suburban and rural settlements surrounding cities[40].

Climate model simulations. We used daily Tmax and Tmin outputs from global climate models participating in the Coupled Model Intercomparison Project Phase 6 (CMIP6)[41], including historical simulations forced by anthropogenic plus natural forcings (ALL), greenhouse gases forcing only (GHG), and natural forcings only (NAT; solar activities and volcanic aerosols). To extract the forcing signals through averaging out randomly phased realizations of internal variability, we required each model to have at least three ensemble members providing daily Tmax and Tmin simulations in each forcing experiment. This sorts out eight models (Supplementary Table 4), which also provide projected variables in at least one ensemble member under four CMIP6 Tier— 1 emissions scenarios driven by various socioeconomic assumptions called shared socioeconomic pathways (SSPs) (i.e., SSP1-2.6, SSP2-4.5, SSP3-7.0 and SSP5-8.5). We also used unforced pre-industrial control (piControl) simulations from 17 models.

Mortality records. We used daily counts (00:00–24:00) of non-accidental mortality records in 98 death surveillance points distributed in five provinces (Hebei, Jiangsu, Zhejiang, Sichuan and Guangdong) and four municipalities (Beijing, Tianjin, Shanghai and Chongqing). These surveillance points well cover major urban agglomerations in Eastern China (Supplementary Fig. 10). The mortality records of Zhejiang and Guangdong provinces during 2013–2017 were obtained from the respective Provincial Center for Disease Control and Prevention. Data for other provinces and municipalities during 2006–2011 were collected from Chinese Center for Disease Control and Prevention. These records follow the same reporting and certificating protocols[42]. According to the International Classification of Diseases-10th Revision (ICD-10), non-accidental deaths, coded as A00-R99, resulted from diseases rather than from injuries (traffic related mortalities, suicide, drowning, etc.). Considering that age- and gender-dependent physiological and socio-economic status might alter the community's vulnerability to heat exposure, daily deaths were further grouped by sex and age (0–64, 65–74, and ≥75 years old), respectively. Basic statistics of daily non-accidental deaths are summarized in Supplementary Table 5.

Future population and urban land expansion. We used spatially explicit global urban and rural population projections provided at a spacing of 0.125° for every decade of 2010–2100[43]. This demographic dataset is quantitatively consistent with national population and urbanization projections under different SSPs. We used urban land projections[25] under various SSPs at a spatial resolution of 1 km and decadal intervals for 2020–2100 to estimate future changes in grid-level (5°×5°) urban fraction. The future urban extent was estimated by the 'Future Land-Use Simulation' model, which takes advantage of machine learning and cellular automata to account for population size, urbanization rate (ratio of urban population to total population) and gross domestic product[25].

Definition of summertime hot extremes. We determined a hot day/night when Tmax/Tmin is higher than the 90th percentile of its long-term counterparts (1961–1990). The daily-based percentile was calculated from a time window of 15 days centered on each calendar day over 1961–1990 (i.e., total daily samples: 15×30=450 days). The 90^{th} percentile serves as a proper compromise between the event extremity and sample size for trend analysis, and also captures the possibility of relatively-moderate extremes combining to cause huge impacts.

By the temperature observing and archiving protocol (yesterday's 20:00 to today's 20:00), daily minima appear in the early morning of the day (02:00) and thus precede daily maxima (14:00). That is, the temperature dataset, providing only Tmin and Tmax, under-samples the evening-to-midnight temperatures, but the daily count of mortality is an accumulation from 00:00 to 24:00. To better match the type of hot extremes (exposure) to mortality (after-exposure consequences), we divided a day into three subperiods, i.e., early morning (midnight to sunrise), daytime (sunrise to sunset), and nighttime (sunset to midnight), which are measured by Tmin of the day ($Tmin_0$), Tmax of the day ($Tmax_0$) and Tmin of the next day ($Tmin_1$), respectively. The unavailability of hourly temperature records compels us to take $Tmin_1$ as a surrogate of today's evening-to-midnight temperature, considering the good continuity of temperature within a few hours.

Three types of summertime hot extremes are accordingly defined as: (i) daytime-only hot extreme—an extremely hot day neither preceded nor followed by hot nights (i.e., $Tmax_0>90^{th}$ percentile, $Tmin_0 \leq 90^{th}$ percentile and $Tmin_1 \leq 90^{th}$ percentile); (ii) nighttime-only hot extreme—extremely hot in the early morning or/and in the following night, but normal during daytime (i.e., $Tmax_0 \leq 90^{th}$ percentile, and $Tmin_0$ or/and $Tmin_1>90^{th}$ percentile); (iii) compound hot extreme—sustained hot event combining extremely elevated daytime ($Tmax_0$) and nighttime ($Tmin_0$ or/and $Tmin_1$) temperatures (i.e., $Tmax_0>$90th percentile, and $Tmin_0$ or/and $Tmin_1>90^{th}$ percentile).

Excess mortality attributed to summertime hot extremes. We first employed a distributed lag non-linear model (DLNM) with quasi-Poisson distribution[44] to establish the hot extremes-mortality relationship in each death surveillance point. Daily counts of deaths were considered as the dependent variable, and the occurrence of hot extremes was used as the predictor (days seeing no hot extremes set as reference for comparison and referred to as normal days). We then introduced a cross-basis function in the DLNM to model the non-linear and lag effects of hot extremes on deaths, with the maximum lag set as 1 day[45]. We controlled long-term trends, relative humidity, and the day-of-week effect as potential confounders in the DLNM. We then performed a multivariate meta-regression to pool the location-specific exposure-response association[46]. Observed Tmax and Tmin in the station nearest to the death surveillance location were used to represent surface air temperatures there. In order to test the robustness of our findings, we also conducted sensitivity analysis accounting for 3-, 5- and 7-day lags instead. The shown association as measured by relative risks, calculated by summing contributions at different lags[44], refers to cumulative effects of hot extremes of certain type on mortality over the whole lag period. Technical details of the DLNM model could be found in Supplementary Note 1 and ref. 44.

Considering inconsistent temporal coverage of mortality records from different sources, we also performed additional sensitivity analysis with respect to the entire data collection period and each sub-period, respectively (Supplementary Table 1).

Classification of urban and rural stations. We classified urban and rural stations in Eastern China (15–55°N; 100–135°E) using the LULC maps. Following previous studies[47], we set up a buffer zone of 2 km radius around each station to estimate the fraction of neighbouring built-up areas. We considered a station as an urban one if the built-up land fraction surrounding it is greater than 33%[47]. A station was determined to be rural if its neighbouring built-up fraction remained below 33% throughout the analysis period (1961–2014). Thus, urban stations were dynamically classified over time. By these criteria, only 314 stations across Eastern China were classified into urban in 1980 (Supplementary Fig. 11); while the number reached 972 by 2010 as urbanization accelerated since then[48]. This dynamic classification scheme captures both the expansion of pre-existing cities and the rural-urban transformation (Supplementary Fig. 10), thus better characterizing the forcing from regional urbanization processes.

Urban-rural contrast in summertime hot extremes. To estimate the urban-rural difference in frequency of hot extremes, we divided Eastern China into thirty 5° ×5° latitude-longitude grid cells. For each grid cell, we first calculated the event frequency at individual stations, and then arithmetically averaged the frequency amongst all urban (rural) stations within that grid to derive the grid-level urban (rural) frequency. To eliminate potential topographical effects on grid values, we excluded the stations whose altitude became 500m higher than the lowest station within the same grid during the rural-urban transformation. Further, we constructed urban-/rural-mean frequency series of summertime hot extremes by averaging grid values of urban/rural frequency weighted by the cosine of their central latitudes.

Stepwise detection and attribution. We re-gridded the model outputs onto 5° ×5° grid cells using the bilinear interpolation algorithm, and masked the model grids by the gridded observation network (Supplementary Fig. 2a). For each simulation, we calculated the grid-level frequency of summertime hot extremes as did in observations. Considering spatially heterogenous levels of urbanization and aerosol concentrations, we divided Eastern China into three sub-regions: southeastern China (15–30°N; 100–125°E), central-eastern China (30–40°N; 100–125°E) and northeastern China (40–55°N; 100–135°E). With respect to each of them, we prepared area-weighted mean frequency series for the space-time fingerprinting analysis.

We used total least squares-based optimal fingerprinting[49,50] to detect and attribute spatiotemporal changes of summertime compound hot extremes over Eastern China. This approach considers the observed change as a linear combination of scaled noisy fingerprints of various external forcings (**X**; the spatiotemporal responsive patterns to specific forcings). Given no urbanization effect in both the rural series and the CMIP simulations, we first regressed observed rural-mean frequency changes ($\mathbf{Y}_{OBS\_R}$) onto the simulated space-time responses to anthropogenic (ANT; $\mathbf{X}_{ANT}$) and natural (NAT; $\mathbf{X}_{NAT}$) forcings in a two-signal analysis:

$$\mathbf{Y}_{OBS\_R}=\beta_{ANT}(\mathbf{X}_{ANT}-\mathbf{u}_{ANT})+\beta_{NAT}(\mathbf{X}_{NAT}-\mathbf{u}_{NAT})+\mathbf{u}_0 \quad (1)$$

where β is the scaling factor for the fingerprint of subscript-specified forcings, and $\mathbf{u}$ in the bracket represent the noise (uncertainty) component of $\mathbf{X}$. $\mathbf{u}_0$ is the internally generated residual variability. The elements in Eq. (2)-(4) are the same to those in Eq. (1), but for different forcings. $\mathbf{X}_{ANT}$ was estimated as the difference between multi-model ensemble (MME) responses to ALL and to NAT forcings.

We also conducted a three-signal analysis to disentangle the contributions from individual forcing agents, including GHG, other anthropogenic forcings (OANT; predominately anthropogenic aerosols and large-scale land use changes) and NAT forcings, to rural-mean changes. We regressed observed spatiotemporal changes in rural areas ($\mathbf{Y}_{OBS\_R}$) simultaneously onto the space-time fingerprints of GHG ($\mathbf{X}_{GHG}$), OANT ($\mathbf{X}_{OANT}$) and NAT ($\mathbf{X}_{NAT}$):

$$\mathbf{Y}_{OBS\_R}=\beta_{GHG}(\mathbf{X}_{GHG}-\mathbf{u}_{GHG})+\beta_{OANT\_R}(\mathbf{X}_{OANT}-\mathbf{u}_{OANT})+\beta_{NAT}(\mathbf{X}_{NAT}-\mathbf{u}_{NAT})+\mathbf{u}_0 \qquad (2)$$

where β_{OANT_R} is scaling factor of OANT for rural areas, and $\mathbf{X}_{OANT}$ was estimated as the difference between the ALL- and GHG+NAT-forced MME responses.

Assuming negligibly small difference in GHG and NAT forcings on rural- and urban-mean hot extremes at the scale as large as Eastern China, we removed frequency changes attributable to large-scale external forcings (i.e., $\beta_{GHG}\mathbf{X}_{GHG}+\beta_{NAT}\mathbf{X}_{NAT}$) in the observed urban series ($\mathbf{Y}_{OBS\_U}$):

$$\mathbf{Y}_{OBS\_U}=\beta_{GHG}(\mathbf{X}_{GHG}-\mathbf{u}_{GHG})+\beta_{OANT\_U}(\mathbf{X}_{OANT}-\mathbf{u}_{OANT})+\beta_{NAT}(\mathbf{X}_{NAT}-\mathbf{u}_{NAT})+\beta_{URB}(\mathbf{X}_{URB}-\mathbf{u}_{URB})+\mathbf{u}_0 \qquad (3)$$

The residual frequency changes ($\mathbf{Y}_{RES}$) were expressed as a sum of the scaled fingerprints of OANT ($\mathbf{X}_{OANT}$) and the urbanization forcing (URB; $\mathbf{X}_{URB}$):

$$\mathbf{Y}_{RES}=\beta_{OANT\_U}(\mathbf{X}_{OANT}-\mathbf{u}_{OANT})+\beta_{URB}(\mathbf{X}_{URB}-\mathbf{u}_{URB})+\mathbf{u}_0 \qquad (4)$$

where β_{OANT_U} and β_{URB} are scaling factors of OANT and URB for urban areas.

Obviously, Eq. (4) acknowledges that the urban-rural contrasting frequency of hot extremes is not due purely to urban expansion, but other urban-rural differential forcings (e.g., aerosols and deforestation, OANT) also play a sizable role[13,30]. The uncertainties sourced from the removal of GHG+NAT forcings in estimating the scaling factors in Eq. (4) are detailed in Supplementary Discussion 1.

The ALL, GHG and NAT fingerprints were represented by the MME mean frequency anomalies series, which were derived by averaging multi-member means of each model in the respective forcing experiments. For the urbanization fingerprint (URB), we constructed it by fitting the observed series of urban-rural frequency difference in each sub-region with the logistic sigmoid function, a good simulator of an 'S'-shape process (Fig. 2b and Supplementary Fig. 12). Such a construction of URB fingerprint expects that urbanization-added frequency scales with urban built-up areas that expanded slowly, grew steeply and then plateaued gradually over Eastern China (Supplementary Fig. 12)[23,48,51].

To reduce high frequency variability, we pre-processed the 54-year domain-averaged observational vectors (i.e., $\mathbf{Y}_{OBS\_R}$ and $\mathbf{Y}_{OBS\_U}$) and fingerprint series (i.e., $\mathbf{X}_{ANT}$, $\mathbf{X}_{NAT}$, $\mathbf{X}_{GHG}$, $\mathbf{X}_{OANT}$ and $\mathbf{X}_{URB}$) for each sub-region into non-overlapping 3-year-mean frequency series (i.e., 18 samples). Concatenating three sub-region series successively produced a 54-dimensional observational series and a set of 54-dimensional fingerprints that characterized the space-time response patterns used in Eqs. (1), (2), and (4). We also repeated these calculations by using non-overlapping five-year-mean series (11 samples, i.e., 10 five-year averages plus the average of four additional years) instead.

To solve the above regression models and also conduct residual consistency test, we used the outputs of unforced piControl simulations to construct two independent estimates for inversed variance-covariance matrix of the internal variability (C_N^{-1}), each of which comprised 89 non-overlapping segments with equal length to the analysis period (Supplementary Table 4). By design, the internal variability-related sampling uncertainty of fingerprints is inversely proportional to the number of model runs driven by specific forcings. Whilst, given no urbanization-forced experiment, the URB fingerprint was constructed purely by observation via fitting urban-rural frequency differences. This practice smoothed out most internal variability, and consequently the associated sampling uncertainty was reasonably small. This motived us to artificially specify very large number of "model runs" (i.e., 1,000), in the calculation, to estimate the URB scaling factor. Additional sampling uncertainty in the URB signal related to the station selection and classification are detailed in Supplementary Discussion 2 and shown in Supplementary Fig. 12.

A certain external forcing is deemed detectable in observed changes if the uncertainty range of its scaling factor excludes zero. If the uncertainty range encompasses the unity, the forced pattern is considered consistent with the observation. We conducted a standard residual consistency test to check the validity of the regression fitting. Passing this test means the estimated residuals in the regression models is generally consistent with the assumed internal variability in magnitude. All the regression models used have passed this test at the 0.05 significance level. Based on it, we quantified frequency changes attributable to a given external forcing by multiplying the linear trend of the corresponding fingerprint with the scaling factor (best estimate and uncertainty range).

Observationally constrained projections. Assuming that the historical overestimation/underestimation in the responsive changes (signified by below-unity/above-unity scaling factors) would propagate into the future, we leveraged the attribution results to constrain projections. For the historical period, we reconstructed the simulated frequency anomalies (relative to 1961–2014) of urban compound hot extremes by summing the optimally scaled (multiply respective scaling factors) signals of GHG, OANT, NAT and URB. For the future period (after 2014), we similarly scaled the raw projections of MME mean frequency anomalies and the raw projections of future urbanization-added frequency, by the scaling factors of ANT and URB (see the section below). These optimally scaled future responses were then added up, and further adjusted by the magnitude of difference between the reconstructed and observed historical means (Fig. 4a).

Population exposure to summertime compound hot extremes. We projected population exposure to summertime compound hot extremes, in the unit of person-days, by multiplying the number of events with the number of people exposed. Specifically, for urban/rural areas in each 5°×5° grid, we calculated the decadal-mean frequency (e.g., 2005–2014 for the 2010s, 2015–2024 for the 2020s, and so on) of compound hot extremes and multiplied it by the total urban/rural population in that grid cell for the decade. Raw projections of compound hot extremes do not account for frequency increases due to future urban expansion. Hence, we added this part to the raw predictions of heat hazards, and multiplied the result by grid-level urban population.

Considering a quasi-linear relationship between urbanization-induced warming and city size[52-54] as well as potential nonlinear interactions between urban heat islands and hot extremes[31,55], we gave a coarse-grained estimate for future urbanization-induced frequency changes in summertime compound hot extremes under various SSPs as:

$$\Delta Uaf_{\mathrm{F}} = \Delta Uaf_{0} \times exp^{(\frac{ULC_{\mathrm{F}}}{ULC_{\mathrm{O}}}-1)} \tag{5}$$

where ΔUaf_{0} is the observed urbanization-induced frequency (abbreviated as Uaf) change in summertime compound hot extremes in each grid cell over 1961–2014; ΔUaf_{F} is the estimate of grid-level frequency changes associated with future urban land expansion; ULC_{O} is the observed urban fraction in each grid cell in 2015 (Supplementary Fig. 13a); ULC_{F} is the projected grid-level urban fraction afterwards (Supplementary Figs. 13b and 13c). Thus, in a given grid cell, if future urban fraction doubles, the urbanization-induced frequency change will be approximately 2.72 times the present value (i.e., e*ΔUaf_{0}). We also adopted a simplified linear form (see Supplementary Discussion 3) of the relationship between urban expansion and urbanization-added frequency for sensitivity tests, and obtained overall consistent estimations (Supplementary Fig. 14). The limitation, suitability, and uncertainty of this estimator are detailed in Supplementary Discussion 3. We computed the MME mean global warming magnitudes in each decade (relative to 1850–1900) by weighting (cosine of latitudes) the re-gridded surface air temperatures from the eight CMIP6 models.

Other statistical methods. For linear trend and its significance, we used the nonparametric Theil-Sen's slope estimator[56] in combination with the Mann-Kendall test[57], with the 90% confidence interval quantified following ref. 58.

We applied the variance inflation factor[27] (VIF) to measure the degree of multicollinearity amongst different fingerprints. The VIF for an independent variable (fingerprint in our case) was calculated by:

$$\mathrm{VIF_i}=\frac{1}{1-{R_i}^2} \tag{6}$$

Where ${R_i}^2$ represents the unadjusted coefficient of determination for the multivariate linear model regressing the i^{th} variable onto the remaining ones. If ${R_i}^2$ equals 0 and hence $\mathrm{VIF_i}$ equals 1, the variance of the i^{th} variable is completely free from influences of the others, i.e., no multicollinearity between the variable and other predictors. In contrast, a high VIF, over 10 in particular, signifies strong multicollinearity that might severely distort the estimate for regression coefficients[28].

Data availability

All the data that support the findings are publicly available. The temperature observations and land use/land cover maps are available at http://data.cma.cn/en/ and https://www.resdc.cn/Datalist1.aspx?FieldTyepID=1,3 (website only available in Chinese), respectively. The CMIP5 and CMIP6 model outputs can be accessed at https://esgf-node.llnl.gov/projects/cmip5/ and https://esgf-node.llnl.gov/projects/cmip6/, respectively. The global projections of future population and urban expansion based on the Shared Socioeconomic Pathways are available at https://sedac.ciesin.columbia.edu/data/set/popdynamics-1-8th-pop-base-year-projection-ssp-2000-2100-rev01 and https://doi.pangaea.de/10.1594/PANGAEA.905890, respectively. The mortality data can be secured through a government data-sharing portal (https://www.phsciencedata.cn/Share/en/index.jsp) or from the provincial mortality surveillance system on registration, or from the corresponding author W. M..

Code availability

All the codes associated with this paper are available from the corresponding author upon reasonable request.

Acknowledgments

We thank the National Meteorological Information Center of the China Meteorological Administration for compiling and homogenizing the observational climatic data, and we appreciate the Data Center for Resources and Environmental Sciences of the Chinese Academy of Sciences for developing the temporally evolving land use/land cover maps. We acknowledge the World Climate Research Programme's Working Group on Coupled Modeling, which coordinated and promoted CMIP5 and CMIP6, and we thank the climate modeling groups for producing and making available their model outputs. We thank B. Jones and B. C. O'Neill for developing the spatially explicit global population projections. We also thank G. Chen, X. Li and X. Liu for sharing the global projections of future urban land expansion. J.W., Y.C., Z.Y., and P.Z. were supported jointly by the National Key Research and Development Program of China (Grant No. 2018YFC1507700) and the Strategic Priority Research Programme of the Chinese Academy of Sciences (Grant No. XDA20020201). G.H. and W.M. were supported by the National Nature Science Foundation of China (Grant No. 42075173) and National Key Research and Development Program of China (Grant No. 2018YFA0606200). S.F.B.T. was funded by the UK-China Research & Innovation Partnership Fund through the Met Office Climate Science for Service Partnership (CSSP) China as part of the Newton Fund.

Author contributions

Y.C., J.W., G.H., S.F.B.T. and W.M. designed the research; J.W., W.L., G.H. and Y.C. performed the analyses; J.W. wrote the draft, and Y.C., J.W. and S.F.B.T. reviewed and edited it; S.F.B.T., Z.Y., P.Z., J.F., W.M., C.H. and Y.H. gave valuable suggestions on the analyses; all authors contributed to the interpretation of the results.

Competing interests

The authors declare no competing interests.

Figure Legends

Fig. 1: Cumulative relative risks (RRs) of mortality associated with three types of summertime hot extremes, with 1-day lag considered. Daily mortality records in urban areas are combined (in blue shading), and grouped by gender (in pink shading) and ages (in green shading). RRs ascribed to different types of hot extremes are represented by colored markers, and the error bars show the 95% confidence interval of estimated RR.

Fig. 2: Urban- and rural-mean frequency anomalies of summertime compound hot extremes in observations and simulations over Eastern China. a, Anomalies (relative to 1961–2014) in frequency. Shown are observations in urban (orange) and rural (green) areas; the multi-model ensemble (MME) mean simulations forced jointly by ANT and NAT forcings (ALL, black) and the 5–95% range of ALL responses among individual simulations (gray shading); and the MME mean responses to NAT forcings (blue) and the corresponding 5–95% range of NAT responses among individual simulations (blue shading). **b**, The differences between urban- and rural-mean frequency (orange dots) and the sigmoid function-fitted pattern of urban-rural difference in the frequency of summertime compound hot extremes (orange dashed line).

Fig. 3: Detection and attribution of frequency changes in summertime compound hot extremes over Eastern China. a, Left panel: best-estimated scaling factors (cross) and their 5–95% uncertainty range (bar) from two-signal space-time optimal fingerprinting analysis for rural-mean series (green); Right panel: those from three-signal analysis for greenhouse gases (GHG), other anthropogenic (OANT) and NAT forcings in rural-mean series (green); and those from two-signal analysis for OANT and urbanization effects (URB) in urban-mean series (orange). **b**, Left panel: best estimates (shaded) and 90% confidence intervals (black bars) of the observed trends for the frequency of summertime compound hot extremes in rural (green) and urban (orange) areas; Right panel: best estimates (shaded) and 5–95% uncertainty range (black bars) of changes

attributable to GHG, NAT and OANT and URB forcings in rural-mean (green) and urban-mean (orange) frequency series.

Fig. 4: Projected changes in frequency of urban compound hot extremes and urban population exposure. a, Left panel: observed (red) and optimally reconstructed (black) changes of urban compound hot extremes over Eastern China; right panel: observationally constrained projections of frequency changes in urban compound hot extremes. The constrained MME mean projections are indicated by thick lines, with the bars framing the 5–95% range for the multi-model ensemble. **b**, Scaling of the observationally constrained decadal-mean frequency of urban compound hot extremes in Eastern China to the decadal-average global mean surface temperature anomalies (GMST, relative to 1850–1900). The blue line shows the linear regression, with the gray shading encompassing its 95% confidence interval. The solid gray lines mark specific levels of global warming at 1.5, 2, and 4 °C and their corresponding decadal-mean event frequencies. The dashed gray line indicates the 1:10 reference scaling between GMST and decadal-mean frequency of extremes. The linear regression model, the proportion of the variance of Y explained by X (R^2), and the Pearson correlation coefficient (corr) alongside its p value (*P*) are also shown. **c**, Changes (relative to the 2010s level) in urban population exposure to summertime compound hot extremes over Eastern China at the middle (2050s; green) and the end (2090s; orange) of the 21st century under various shared socioeconomic pathways. Light- and dark-colored bars represent the MME mean projected exposure changes without and with future urbanization-induced warming effect accounted for, respectively. Vertical black bars encompass the 5–95% range of all members' projections.

References for main text

1. McMichael, A. J., Woodruff, R. E. & Hales, S. Climate change and human health: present and future risks. *Lancet* **367**, 859–869 (2006).
2. Petkova, E. P., Morita, H. & Kinney, P. L. Health impacts of heat in a changing climate: how can emerging science inform urban adaptation planning? *Curr. Epidemiol. Rep*. **1**, 67–74 (2014).
3. Wang, D., Lau, K. K-L., Ren, C. *et al*. The impact of extremely hot weather events on all-cause mortality in a highly urbanized and densely populated subtropical city: A 10-year time-series study (2006–2015). *Sci. Total Environ.* **690**, 923–931 (2019).
4. Karl, T. R. & Knight, R. W. The 1995 Chicago heat wave: how likely is a recurrence? *Bull. Am. Meteorol. Soc.* **78**, 1107–1120 (1997).
5. Kovats, R. S. & Hajat, S. Heat stress and public health: a critical review. *Annu. Rev. Public Health* **29**, 41–55 (2008).
6. Duren, R. M. & Miller, C. E. Measuring the carbon emissions of megacities. *Nat. Clim. Chang.* **2**, 560–562 (2012).
7. Gu, C., Guan, W. & Liu, H. Chinese urbanization 2050: SD modeling and process simulation. *Sci. China Earth Sci*. **60**, 1067–1082 (2017).
8. Chen, Y. & Zhai, P. Revisiting summertime hot extremes in China during 1961–2015: overlooked compound extremes and significant changes. *Geophys. Res. Lett.* **44**, 5096–5103 (2017).
9. Liao, W., Li, D., Malyshev, S. *et al*. Amplified increases of compound hot extremes over urban land in China. *Geophys. Res. Lett*. **48**, e2020GL091252 (2021).
10. Yang, J., Zhou, M., Ren, Z. *et al.* Projecting heat-related excess mortality under climate change scenarios in China. *Nat. Commun.* 12, 1039 (2021).
11. Stott, P. A., Gillett, N. P., Hegerl, G. C. *et al*. Detection and attribution of climate change: a regional perspective. *Wiley Interdiscip. Rev. Clim. Change* **1**, 192–211 (2010).

12. Wang, J., Yan, Z., Li, Z. *et al*. Impact of urbanization on changes in temperature extremes in Beijing during 1978–2008. *Chin. Sci. Bull*. **58**, 4679–4686 (2013).

13. Han, W., Li, Z., Wu, F. *et al*. The mechanisms and seasonal differences of the impact of aerosols on daytime surface urban heat island effect. *Atmos. Chem. Phys.* **20**, 6479–6493 (2020).

14. Kong, D., Gu, X., Li, J. *et al*. Contributions of global warming and urbanization to the intensification of human-perceived heatwaves over China. *J. Geophys. Res. Atmos.* **125**, e2019JD032175 (2020).

15. Sun, Y., Zhang, X., Ren, G. *et al*. Contribution of urbanization to warming in China. *Nat. Clim. Chang.* **6**, 706–709 (2016).

16. Yan, Z., Ding, Y., Zhai, P. *et al*. Re-assessing climatic warming in China since 1900. *J. Meteor. Res.* **34**, 243–251 (2020).

17. Mazdiyasni, O., AghaKouchak, A., Davis, S. J. *et al*. Increasing probability of mortality during Indian heat waves. *Sci. Adv.* **3**, e1700066 (2017).

18. Baccini, M., Biggeri, A., Accetta, G. *et al*. Heat effects on mortality in 15 European cities. *Epidemio*. **19**, 711–719 (2008).

19. Murage, P., Hajat, S. & Kovats, R. S. Effect of night-time temperatures on cause and age-specific mortality in London. *Environ. Epidemiol*. **1**, e005 (2017).

20. Thomas, N. P., Bosilovich, M. G., Collow, A. B. M. *et al*. Mechanisms associated with daytime and nighttime heat waves over the contiguous United States. *J. Appl. Meteorol. Climatol.* **59**, 1865–1882 (2020).

21. Xue, W., Guo, J., Zhang, Y. *et al*. Declining diurnal temperature range in the North China Plain related to environmental changes. *Clim. Dyn.* **52**, 6109–6119 (2019).

22. Wu, L., Feng, J. & Miao, W. Simulating the impacts of irrigation and dynamic vegetation over the North China Plain on regional climate. *J. Geophys. Res. Atmos.* **123**, 8017–8034 (2018).

23. Schneider, A. & Mertes, C. M. Expansion and growth in Chinese cities, 1978–2010. *Environ. Res. Lett.* **9**, 024008 (2014).

24. Graham, M. H. Confronting multicollinearity in ecological multiple regression. *Ecology* **84**, 2809–2815 (2003).

25. Chen, G., Li, X., Liu, X. *et al*. Global projections of future urban land expansion under shared socioeconomic pathways. *Nat. Commun.* **11**, 537 (2020).

26. Taylor, K. E., Stouffer, R. J. & Meehl, G. A. An overview of CMIP5 and the experiment design. *Bull. Am. Meteorol. Soc.* **93**, 485–498 (2012).

27. Marquaridt, D. W. Generalized inverses, ridge regression, biased linear estimation, and nonlinear estimation. *Technometrics* **12**, 591–612 (1970).

28. Vittinghoff, E., Glidden, D. V., Shiboski, S. C. *et al*. Regression methods in biostatistics: linear, logistic, survival, and repeated measures models. *New York: Springer* (2012).

29. Li, D., Liao, W. L., Rigden, A. J. *et al*. Urban heat island: Aerodynamics or imperviousness? *Sci. Adv.* **5**, eaau4299 (2019).

30. Wang, Z., Lin, L., Xu, Y. *et al*. Incorrect Asian aerosols affecting the attribution and projection of regional climate change in CMIP6 models. *npj Clim. Atmos. Sci.* **4**, 2 (2021).

31. Li, D. & Bou-Zeid, E. Synergistic interactions between urban heat islands and heat waves: The impact in cities is larger than the sum of its parts. *J. Appl. Meteorol. Climatol*. **52**, 2051–2064 (2013).

32. Miralles, D. G., Teuling, A. J., van Heerwaarden, C. C. & de Arellano, J. V. Mega-heatwave temperatures due to combined soil desiccation and atmospheric heat accumulation. *Nature Geosci.* **7**, 345–349 (2014).

33. Horton, D. E., Johnson, N. C., Singh, D. *et al*. Contribution of changes in atmospheric circulation patterns to extreme temperature trends. *Nature* **522**, 465–469 (2015).

34. Shepherd, T. G. Atmospheric circulation as a source of uncertainty in climate change projections. *Nature*

Geosci. **7**, 703–708 (2014).

35. Davis, R. E., Hondula, D. M. & Patel, A. P. Temperature observation time and type influence estimates of heat-related mortality in seven U.S. cities. *Environ. Health Perspect*. **124**, 795–804 (2016).
36. Nicholls, N., Skinner, C., Loughnan, M. & Tapper, N. A simple heat alert system for Melbourne, Australia. *Int. J. Biometeorol*. **52**, 375–384 (2008).

References for methods

37. Xu, W., Li, Q., Wang, X. L., *et al*. Homogenization of Chinese daily surface air temperatures and analysis of trends in the extreme temperature indices. *J. Geophys. Res. Atmos*. **118**, 9708–9720 (2013).
38. Wang, X. L. & Feng, Y. RHtestsV3 user manual. *Climate Research Division, Atmospheric Science and Technology Directorate, Science and Technology Branch, Environment Canada, Toronto, Canada*, 28 pp (2010). http://cccma.seos.uvic.ca/ETCCDMI/software.shtml
39. Liu, J., Kuang, W., Zhang, Z. *et al*. Spatiotemporal characteristics, patterns, and causes of land-use changes in China since the late 1980s. *J. Geograp. Sci.* **24**, 195–210 (2014).
40. Liu, J., Zhang, Z., Xu, X. *et al*. Spatial patterns and driving forces of land use change in China during the early 21st century. *J. Geogr. Sci.* **20**, 483–494 (2010).
41. Eyring, V., Bony, S., Meehl, G. A. *et al*. Overview of the Coupled Model Intercomparison Project Phase 6 (CMIP6) experimental design and organization. *Geosci. Model Dev.* **9**, 1937–1958 (2016).
42. Liu, T., Zhou, C., Zhang, H. *et al*. Ambient temperature and years of life lost: A national study in China. *The Innov*. **2**, 100072 (2021).
43. Jones, B. & O'Neill, B. C. Spatially explicit global population scenarios consistent with the Shared Socioeconomic Pathways. *Environ. Res. Lett.* **11**, 084003 (2016).
44. Gasparrini, A., Armstrong, B. & Kenward, M. G. Distributed lag non-linear models. *Stat. Med*. **29**, 2224–2234 (2010).

45. Ye, X., Wolff, R., Yu, W. *et al*. Ambient temperature and morbidity: a review of epidemiological evidence. *Environ. Health Perspect.* **120**, 19–28 (2012).

46. Gasparrini, A. & Armstrong, B. Reducing and meta-analysing estimates from distributed lag non-linear models. *BMC Med. Res. Methodol.* **13**, 1 (2013).

47. Liao, W., Liu, X., Li, D. *et al*. Stronger contributions of urbanization to heat wave trends in wet climates. *Geophys. Res. Lett.* **45**, 11,310–11,317 (2018).

48. Chen, M., Liu, W. & Tao, X. Evolution and assessment on China's urbanization 1960–2010: Under-urbanization or over-urbanization? *Habitat Int.* **38**, 25–33 (2013).

49. Allen, M. R. & Stott, P. A. Estimating signal amplitudes in optimal fingerprinting, part I: theory. *Clim. Dyn.* **21**, 477–491 (2003).

50. Ribes, A., Planton, S. & Terray, L. Application of regularised optimal fingerprinting to attribution. Part I: method, properties and idealised analysis. *Clim. Dyn.* **41**, 2817–2836 (2013).

51. Liu, X., Hu, G., Ai, B. *et al*. Simulating urban dynamics in China using a gradient cellular automata model based on S-shaped curve evolution characteristics. *Int. J. Geogr. Inf. Sci.* **32**, 73–101 (2017).

52. Yuan, F. & Bauer, M. E. Comparison of impervious surface area and normalized difference vegetation index as indicators of surface urban heat island effects in Landsat imagery. *Remote Sens. Environ*. **106**, 375–386 (2007).

53. Zhou, D., Zhang, L., Hao, L. *et al*. Spatiotemporal trends of urban heat island effect along the urban development intensity gradient in China. *Sci. Total Environ*. **544**, 617–626 (2016).

54. Wang, J., Tett, S. F. B. & Yan, Z. Correcting urban bias in large-scale temperature records in China, 1980–2009. *Geophys. Res. Lett*. **44**, 401–408 (2017).

55. An, N., Dou, J., González-Cruz, J. E. *et al.* An observational case study of synergies between an intense heat wave and the urban heat island in Beijing. *J. Appl. Meteorol. Climatol.* **59**, 605–620 (2020).

56. Sen, P. K. Estimates of the regression coefficient based on Kendall's tau. *J. Am. Stat. Assoc.* **63**, 1379–1389 (1968).

57. Kendall, M. G. *Rank Correlation Methods* (Griffin, London, 1975).

58. Hollander, M. & Wolfe, D. in *Nonparametric Statistical Methods*. Ch. **9**, 207–208 (John Wiley & Sons, New York, Sydney, Tokyo-Mexico City, 1973).

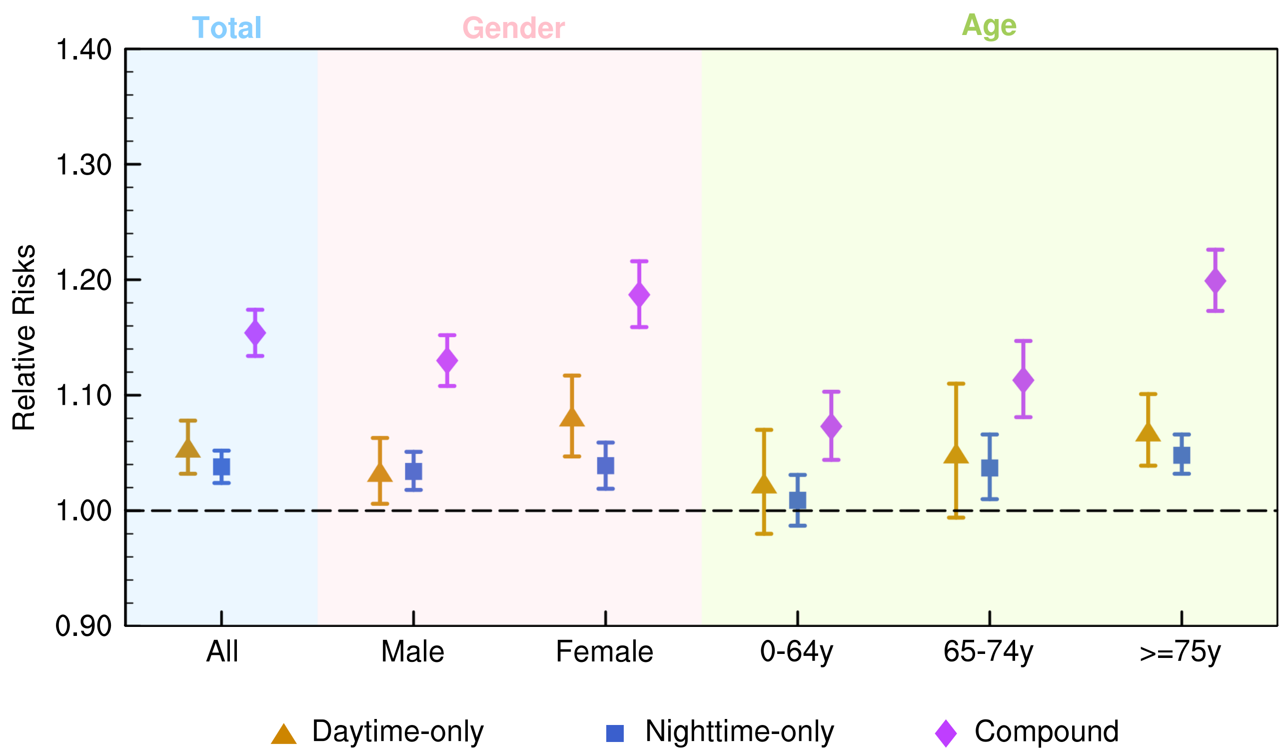

Total
Gender
Age
1.40
1.30
1.20
1.10
1.00
0.90
Relative Risks
All
Male
Female
0-64y
65-74y
>=75y
Daytime-only
Nighttime-only
Compound

a

b

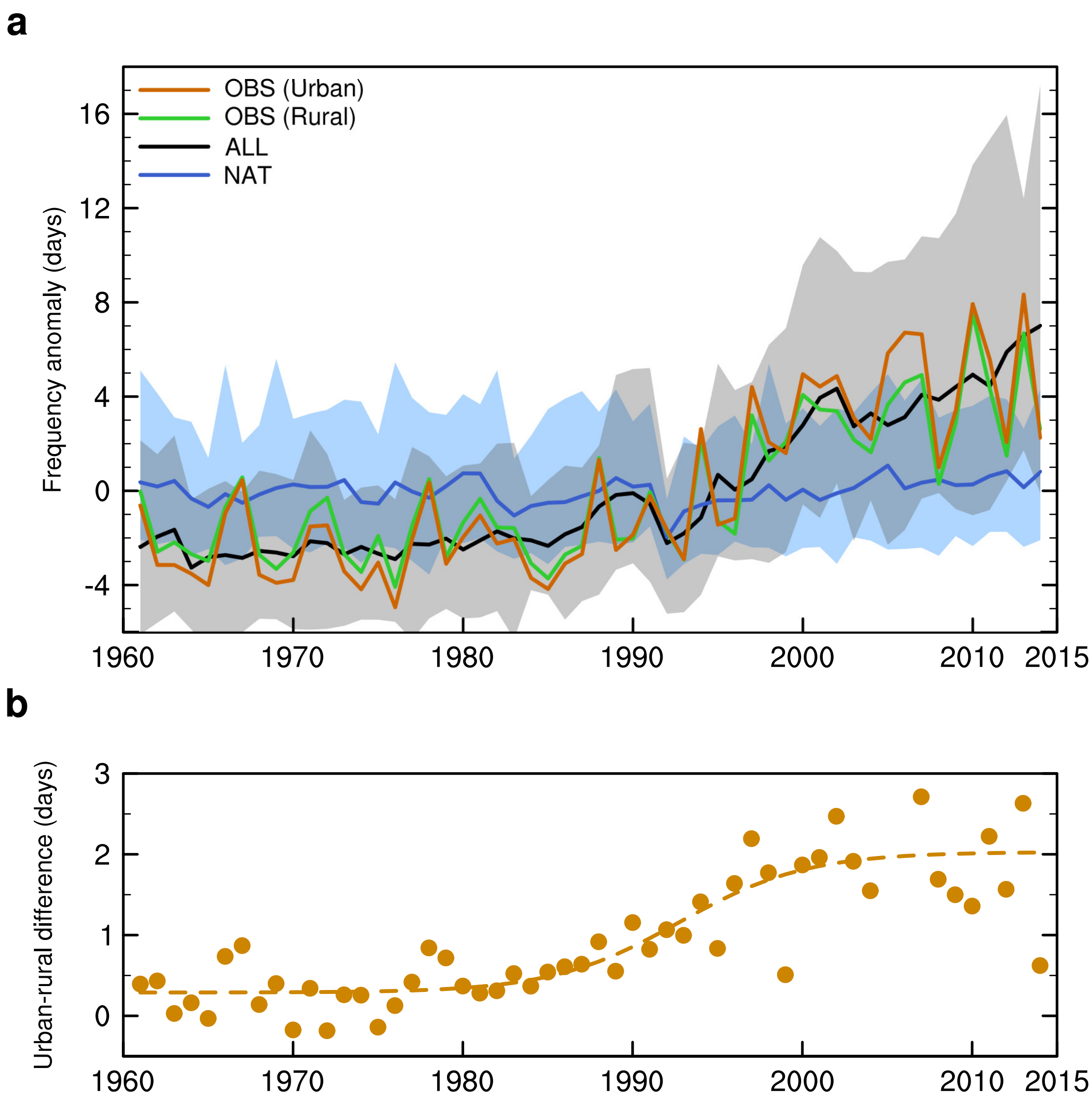

OBS (Urban)
OBS (Rural)
ALL
NAT
Frequency anomaly (days)
16
12
8
4
0
-4
1960
1970
1980
1990
2000
2010
2015
Urban-rural difference (days)
3
2
1
0
1960
1970
1980
1990
2000
2010
2015

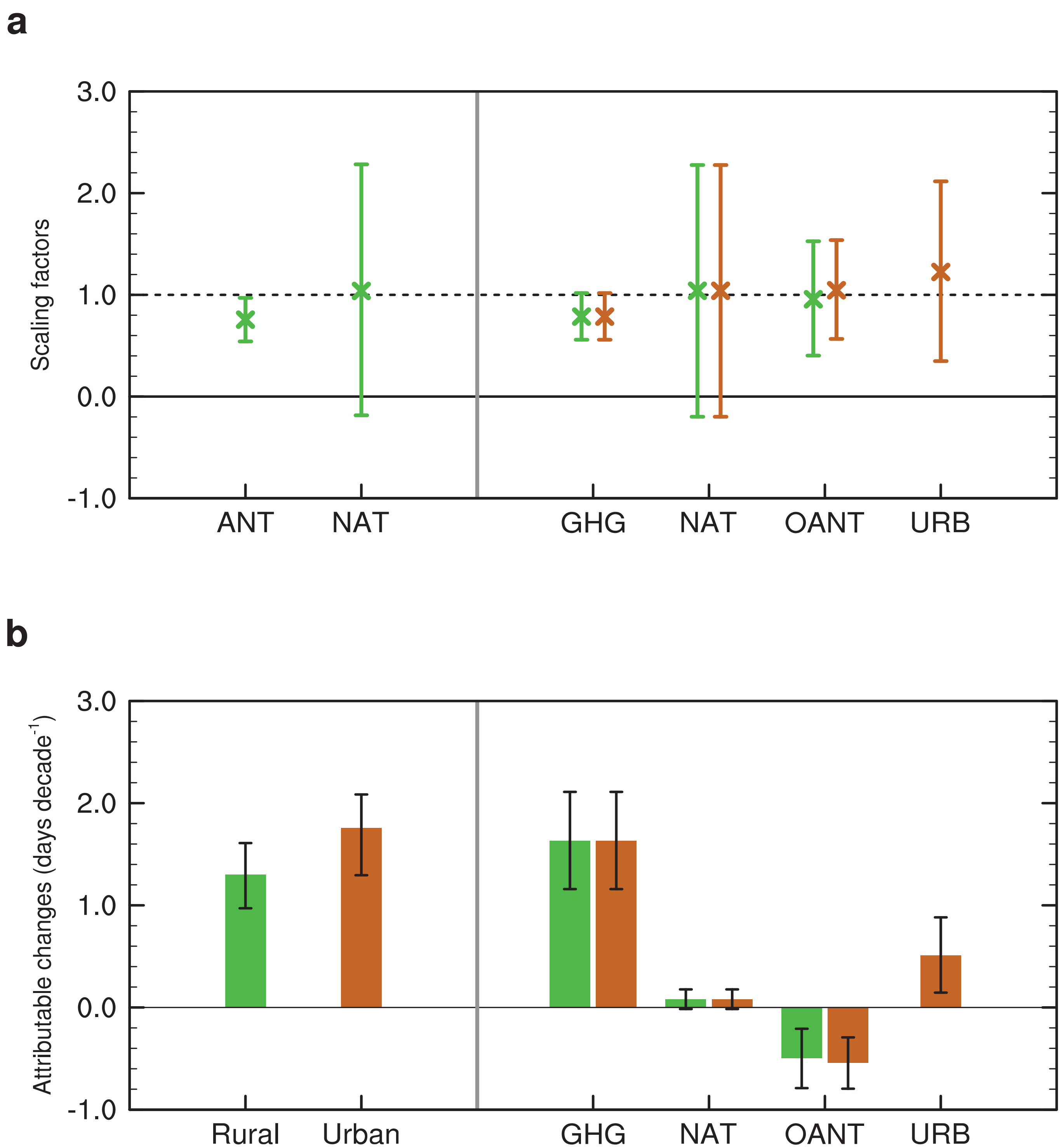

a
3.0
2.0
1.0
0.0
-1.0
Scaling factors
ANT
NAT
GHG
NAT
OANT
URB
b
3.0
2.0
1.0
0.0
-1.0
Attributable changes (days decade^{-1})
Rural
Urban
GHG
NAT
OANT
URB

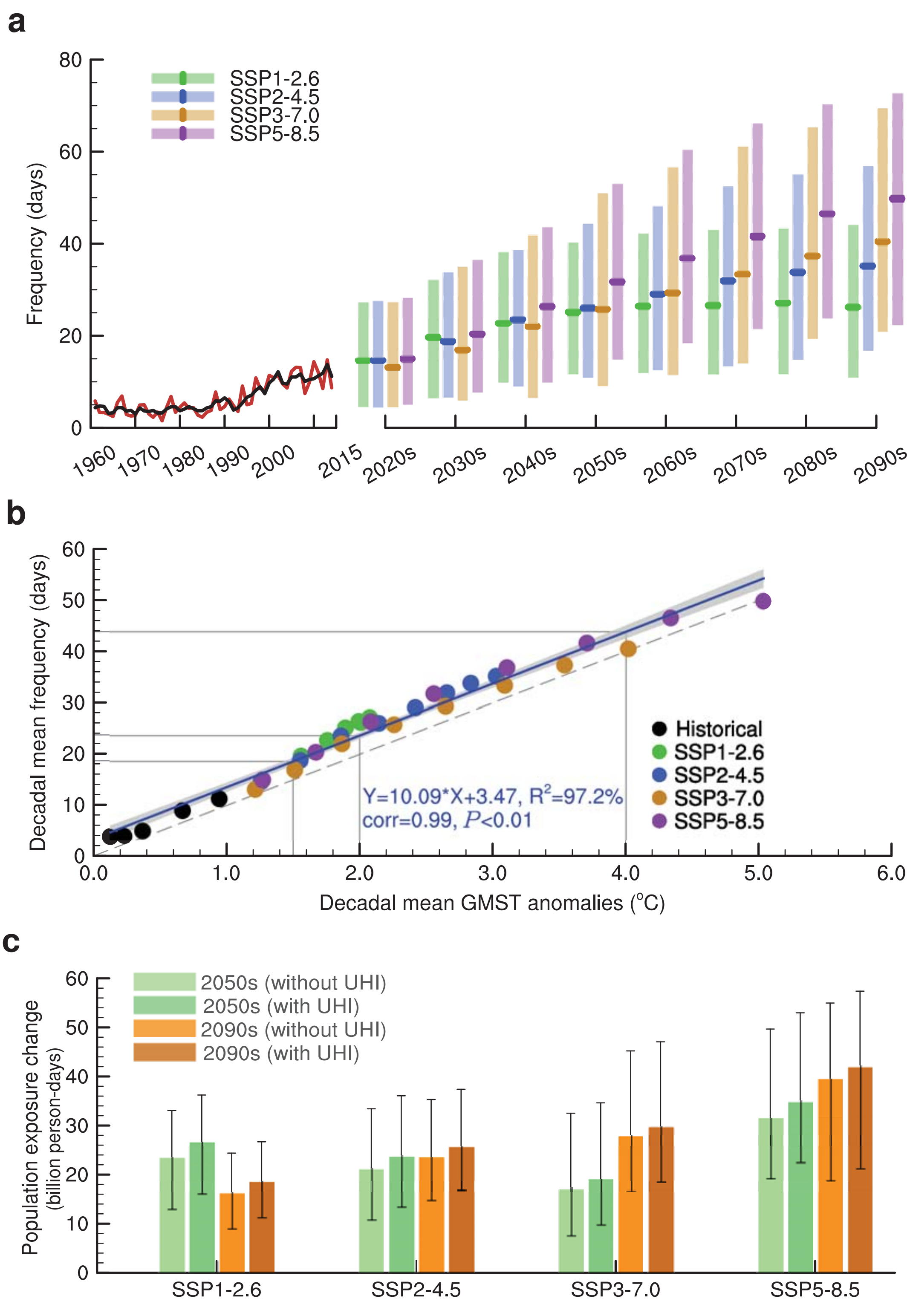

a
SSP1-2.6
SSP2-4.5
SSP3-7.0
SSP5-8.5
Frequency (days)
0
20
40
60
80
1960
1970
1980
1990
2000
2015
2020s
2030s
2040s
2050s
2060s
2070s
2080s
2090s
b
Decadal mean frequency (days)
Historical
SSP1-2.6
SSP2-4.5
SSP3-7.0
SSP5-8.5
Y=10.09*X+3.47, R²=97.2%
corr=0.99, P<0.01
Decadal mean GMST anomalies (°C)
0.0
1.0
2.0
3.0
4.0
5.0
6.0
c
2050s (without UHI)
2050s (with UHI)
2090s (without UHI)
2090s (with UHI)
Population exposure change
(billion person-days)
SSP1-2.6
SSP2-4.5
SSP3-7.0
SSP5-8.5